Contents lists available at ScienceDirect

Transactions of Nonferrous Metals Society of China

36(2026) 433−450

www.tnmsc.cn

Microstructure and properties of HPDC AM60 based alloys for super-sized integrated automotive components

Jing WANG [a,b,#], Xin GUO [a,b,#], Jiang-feng SONG [a,b,*], Dang-he SHI [c], He-cong XIE [a,b], Chun-yu LI [a,b], Heng-rui HU [a,b], Gong CHEN [a,b], Bin JIANG [a,b,**], Dong-xia XIANG [d], Fu-sheng PAN [a,b]

[a] National Engineering Research Center for Magnesium Alloys, Chongqing University, Chongqing 400044, China;
[b] National Key Laboratory of Advanced Casting Technologies, Chongqing University, Chongqing 400044, China;
[c] Vehicle Tech Platform, Seres Auto Co. Ltd., Chongqing 401332, China;
[d] Chongqing Advanced Light Metal Research Institute, Chongqing 400044, China

Abstract: The commercial AM60 (Mg−6Al−0.3Mn) die-casting alloy was modified through Mn, Ce, and La micro-alloying, each at a content below 0.2 wt.%. SEM, TEM, and Micro-CT were employed to characterize the microstructures and properties of AM60 based alloys. AM60-0.2La alloy showed excellent mechanical properties. The ultimate tensile strength, yield strength, and elongation of (288.0±1.7) MPa, (158.0±1.0) MPa, and (22.0±3.0)% were achieved in AM60-0.2La alloy. Besides, AM60-0.2La alloy exhibited the best corrosion resistance (0.29 mm/a) and fluidity among the investigated four alloys. The excellent mechanical properties and corrosion resistance are mainly attributed to the grain refinement strengthening, low porosity, and low content of large shrinkage porosity, promising for super-sized integrated automotive components.

Keywords: magnesium alloys; microstructure; mechanical properties; high-pressure die-casting; integrated automotive components

1 Introduction

The electric vehicle (EV) industries have been developed rapidly in recent years [1,2]. EVs have a higher demand for light-weighting than internal combustion engine vehicles due to the extra weight of batteries [3]. Among the lightweight solutions, integrated magnesium alloy high-pressure die-casting (HPDC) super-sized automotive parts emerge as one of the best solutions. Tesla integrated 171 complex vehicle components into two integrated aluminum alloy Giga castings, significantly reduced the weight by 30%, and lowered the cost by 40%. In addition, substituting aluminum alloys with magnesium alloys can further reduce the weight by around 30% since the density of magnesium alloys is only 2/3 that of aluminum alloys.

In 2023, the National Magnesium Alloy Engineering Research Center (CCMg) of Chongqing University, in cooperation with Chongqing MilliSon Technology Co., Ltd. and Chongqing Boao Magnesium & Aluminum Manufacturing Co., Ltd., successfully produced the most oversized magnesium alloy super-sized integrated HPDC automotive part in the world, with a projection area of exceeding 2.2 m^2 using a MilliSon 8800T die-casting system. The castings are 32% lighter than the original aluminum alloy casting, demonstrating an excellent potential for light-weighting applications

# Jing WANG and Xin GUO contributed equally to this work
Corresponding author: *Jiang-feng SONG, Tel: +86-182023616225, E-mail: jiangfeng.song@cqu.edu.cn;
**Bin JIANG, Tel: +86-13594190166, E-mail: jiangbinrong@cqu.edu.cn
https://doi.org/10.1016/S1003-6326(25)66974-3
Received 28 May 2024; accepted 3 March 2025

in the automotive industry. The integrated die-casting of super-large automotive parts is attracting much attention, a significant trend in the future development of lightweight EVs [4].

Due to the complexity and extended flow distance of super-sized automotive components, HPDC magnesium alloys must exhibit good fluidity and excellent mechanical properties without requiring heat treatment. Additionally, these alloys need to possess good corrosion resistance and be cost-effective for widespread application in EVs.

In recent years, several high-performance HPDC magnesium alloys have been developed. However, few HPDC magnesium alloys exhibited both high strength and high plasticity. ZHANG et al [5] reported that the AM40-4La alloy exhibited room temperature (RT) yield strength (YS), ultimate tensile strength (UTS), and elongation (EL) of 155 MPa, 265 MPa, and 12%, respectively. LV et al [6] developed a high-performance HPDC Mg−4Al−3La−2Gd−0.3Mn alloy with YS, UTS, and EL at RT of 181 MPa, 284 MPa, and 14%, respectively. Researchers also attempt to develop high-performance HPDC magnesium alloys with high rare earth (RE) content. HPDC Mg−11Gd−3Y−1Zn−0.2Zr alloy developed by CHANG et al [7] showed a YS, UTS, and EL of (246±12) MPa, (285±14) MPa, and (3.4±0.4)%, respectively. The HPDC Mg−6Y−3Zn−1Al alloy exhibited a YS of 175 MPa, a UTS of 281 MPa, and an EL of 9.8% [8]. However, the listed alloys contain a medium or high content of RE, leading to high cost and generally poor fluidity, which is unsuitable for integrated die-casting of super-sized automotive parts [9,10]. Therefore, developing new low-cost magnesium alloys with high strength and plasticity is necessary.

To reduce the cost and enhance the fluidity of magnesium alloys for super-sized automotive component applications, we designed new HPDC magnesium alloys with the small addition of low-cost Mn, Ce, and La elements to commercial AM60 alloy in this study. The microstructures and properties of four HPDC alloys, namely AM60 (Mg−6Al−0.3Mn), AM61 (Mg−6Al−0.5Mn), AM60-0.2Ce (Mg−6Al−0.3Mn−0.2Ce), and AM60-0.2La (Mg−6Al−0.3Mn−0.2La), were investigated. The impact of Mn, Ce, and La addition on the grain size, pore morphology, porosity, fluidity, mechanical properties, and corrosion resistance of the AM60 based alloys was studied.

2 Experimental

2.1 Materials preparation

The nominal compositions of the four alloys studied were Mg−6Al−0.3Mn (AM60), Mg−6Al−0.5Mn (AM61), Mg−6Al−0.3Mn−0.2Ce (AM60-0.2Ce), and Mg−6Al−0.3Mn−0.2La (AM60-0.2La). The chemical compositions of the alloys were determined by Inductively Coupled Plasma Atomic Emission Spectrometry (ICP-AES), and the results are listed in Table 1. Besides, the total content of impurity elements Si and Fe in every alloy was less than 0.05 wt.%.

Table 1 Actual chemical compositions of alloys (wt.%)

Alloy	Al	Mn	Ce	La	Mg
AM60	5.94	0.31	−	−	Bal.
AM61	5.96	0.59	−	−	Bal.
AM60-0.2Ce	5.91	0.25	0.17		Bal.
AM60-0.2La	5.32	0.29	−	0.20	Bal.

The AM60 based alloy castings were first melted in an electric resistance furnace at 720 °C under a protective atmosphere of 1 vol.% SF_6 + 99 vol.% CO_2, using pure Mg (99.99%) along with Mg−10Mn, Mg−30Ce, and Mg−30La (wt.%) master alloys. Specimens were produced using a 650 t clamping force cold chamber die-casting machine (YIZUMID-M650). The metal was hand-ladled into the casting machine at a melt temperature of 720 °C. The mold was equipped with a heating system, and the mold temperature for die-casting was 200 °C. The die-casting process involved a slow shot speed of 0.15 m/s, a fast shot speed of 6 m/s, a casting pressure of 15 MPa, and a boost pressure of 30 MPa. Each alloy was die-cast in 40 molds, with the first five not counted due to parameter instability, such as mold temperature and shot rate. The samples were cooled by natural cooling. The die-casting product is shown in Fig. 1(a).

2.2 Microstructure characterization

A cylindrical specimen, measuring 8 mm in length and 6.4 mm in diameter, was extracted from the middle section of the unstretched tensile bar via wire cutting, as indicated by the red marking in Fig. 1(a). Upon sampling completion, the cross-sectional morphology of the samples was examined

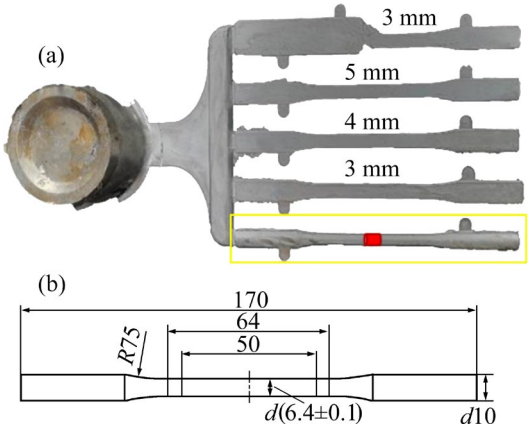

Fig. 1 (a) Casting schematic including top sample for testing corrosion performance, tensile bar with central diameter of 6.4 mm at bottom and three plate samples with thicknesses of 3, 4, and 5 mm, respectively; (b) Dimensions of tensile bar specimen (Unit: mm)

using optical microscopy (OM). The OM samples were ground with SiC abrasive paper (grit sizes ranging from 320# to 4000#) and etched in a picric acid solution (0.85 g picric acid, 2 mL glacial acetic acid, 2 mL ethanol, and 10 mL distilled water) for 10 s. The microstructure was revealed using a ZEISS Axiovert 40 MAT optical microscope.

The secondary phase and pores of the alloys were observed using a scanning electron microscope (SEM, FEI Nova 400). Electron backscattered diffraction (EBSD) analysis was conducted with the SEM to determine the grain size of the samples. The samples were ground with SiC abrasive paper (grit sizes ranging from 320# to 4000#) and then electrolytically polished in AC2 solution at −15 °C, 20 V, and 0.03 A for 40 s. Grain size distribution was analyzed using the Aztec Crystal software.

Additionally, the samples were cut into 10 mm × 10 mm blocks and examined via X-ray diffraction (XRD) using a D/max−2500PC X-ray diffractometer. The XRD analysis was performed by employing a Cu K_α target with an operating current of 40 mA, a voltage of 40 kV, and a scanning speed of 2 (°)/min. The alloy microstructure after tensile deformation was further analyzed using transmission electron microscope (TEM, FEI Talos F200 S). Samples were mechanically ground to a thickness of ~50 μm and then ion-thinned using a GATAN PIPS II 691 instrument.

The three-dimensional characterization of the pores in the red-marked samples shown in Fig. 1(a) was performed using a BRUKER SKYSCAN 1276 Micro-CT. The operating voltage and current were set to be 100 kV and 200 μA, respectively, with an image resolution of 3 μm. The data obtained were reconstructed in three dimensions (3D) using post-processing software such as CT-Analyser and CT-Volume, resulting in a comprehensive three-dimensional pore distribution map. The extracted porosity-related parameters included diameter, volume, and sphericity, etc. In addition, in this study, the Pandat thermodynamic software was employed to calculate the secondary phase content during the solidification process of AM60 based alloys.

2.3 Mechanical performance tests

The tensile samples were taken directly from the tensile bar structure in the mold, as indicated by the markings in the yellow block in Fig. 1(a). The tensile tests were performed after removing the ejector structure on both sides and lightly sanding the surface. The tensile samples had a gauge length of 64 mm and a gauge diameter of 6.4 mm, with other specific dimensions shown in Fig. 1(b). The tensile tests were conducted at RT using a CMT1505 tensile testing machine with a tensile rate of 3.84 mm/min and a strain rate of 0.001 s^{-1}. At least three repeated experiments were performed to ensure data reliability.

2.4 Corrosion resistance test

Specimens for hydrogen evolution tests were cut into cubes with dimensions of 20 mm × 20 mm × 3 mm. The cut samples were sealed with AB glue to expose a test surface area of 400 mm^2, ground to 4000# using SiC paper, cleaned with ethanol, and dried with flowing air. Hydrogen evolution measurements were carried out using an inverted funnel attached to an inverted burette positioned over the specimen, exposing an area of 400 mm^2 in a 3.5 wt.% NaCl solution saturated with $Mg(OH)_2$ at RT to maintain a consistent pH value during the immersion test. The corrosion rate (P_H) (mm/a) was calculated from the hydrogen evolution volume (V_H) (mL/cm^2) and immersion time t (d), using the following equation [11]:

$$P_H=2.088V_H/t \quad (1)$$

3 Results

3.1 Microstructure

The microstructures of the cross-section at the

center of the bar specimens of the four AM60 based alloys are depicted in Fig. 2. The microstructure predominantly comprises refined grains and coarse dendrites interspersed with each other. The cross-section can be divided into three regions: the center, transition, and surface regions, aligned along a narrow band roughly parallel to the casting surface contour. A detailed examination reveals that the center region (Figs. 2(a, d, g, j)) contains coarse dendrites with some equiaxed fine crystals. This region exhibits larger dendrites and numerous aggregates, resulting in significant porosity at the grain boundaries. The transition region exhibits finer dendritic microstructure than the center, with an increasing number of refined equiaxed grains. Moving from the center of the bar specimen through the transition region to the surface layer, the proportion of large dendrites gradually diminishes. The grains are notably refined in the surface region, featuring numerous minor and round α-Mg grains.

The OM results do not effectively characterize the average grain size (AGS) of the alloys due to the presence of numerous refined grains. As shown in Figs. 3(a−l), the EBSD results elucidate the variation in grain size across three distinct regions of the alloys. All regions primarily consist of coarse and refined grains. Coarse grains, identified as externally solidified crystals (ESCs), generally form during filling. In this study, grains with a diameter exceeding 20 μm are recognized as ESCs. The grain size diminishes progressively from the center to the surface, primarily due to reduced ESCs and

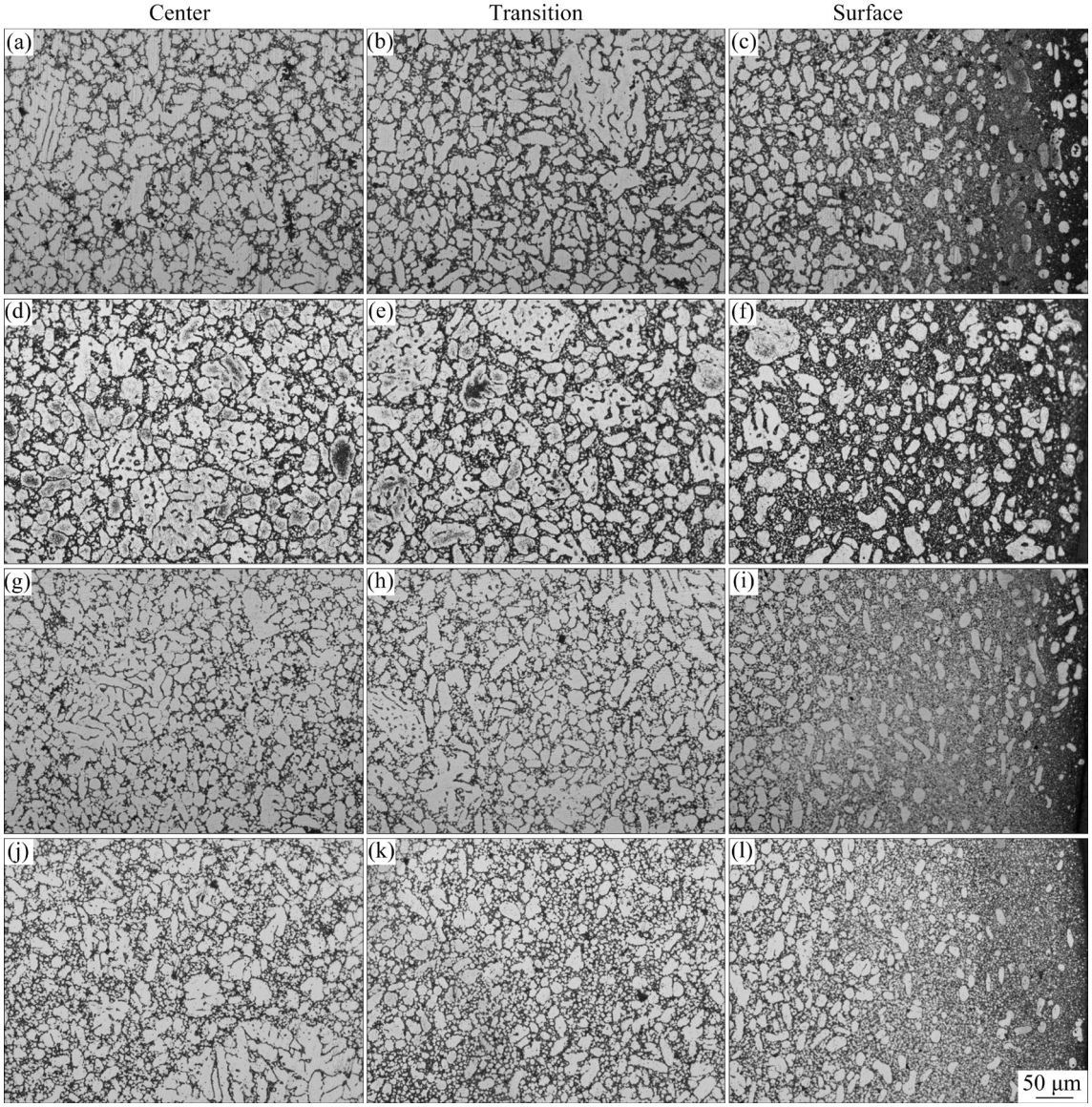

Fig. 2 Microstructures of HPDC AM60 based alloys in different regions: (a−c) AM60; (d−f) AM61; (g−i) AM60-0.2Ce; (j−l) AM60-0.2La

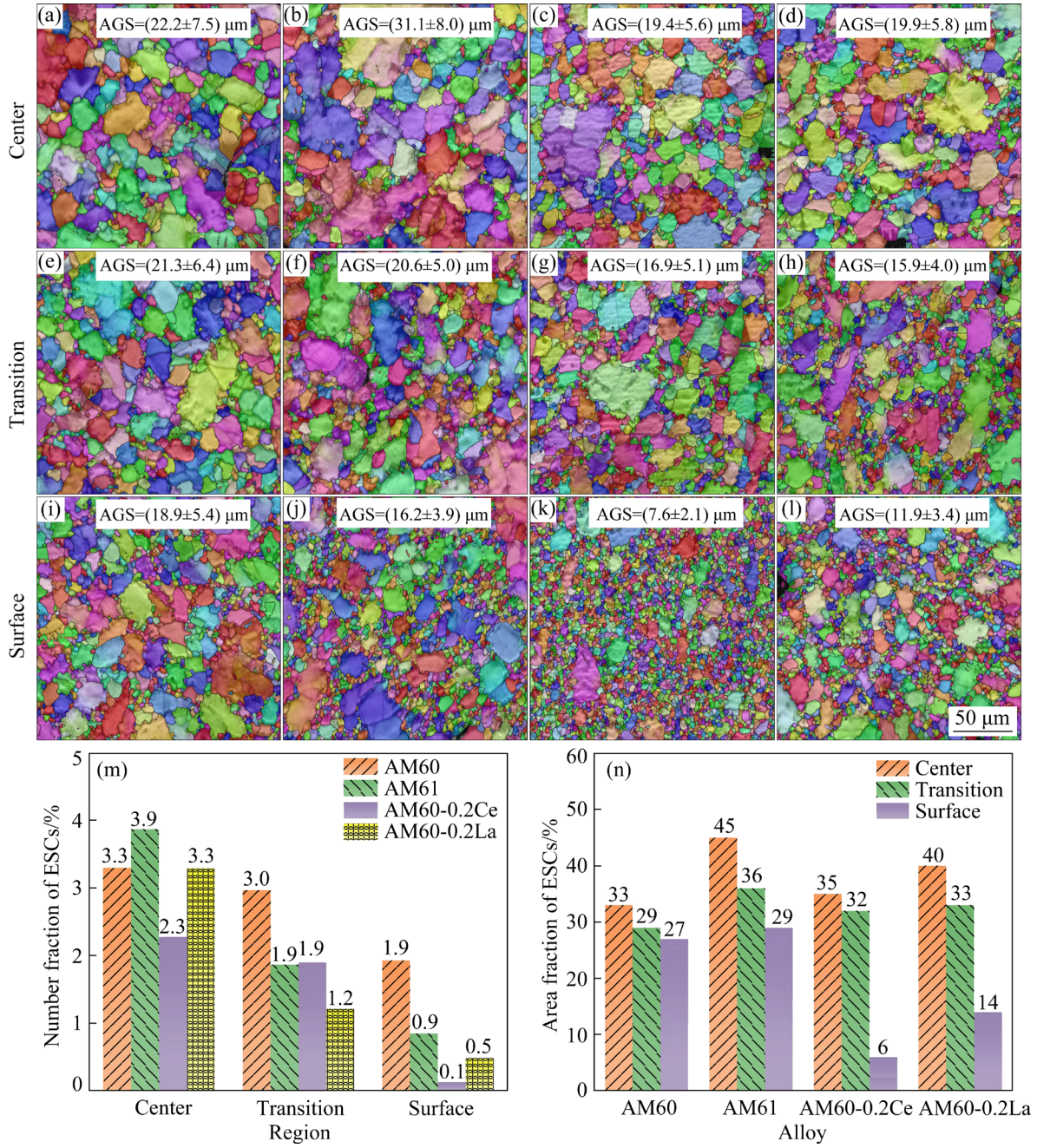

Fig. 3 Variation of average grain size (AGS) of HPDC alloys characterized using EBSD for AM60 (a, e, i), AM61 (b, f, j), AM60-0.2Ce (c, g, k), and AM60-0.2La (d, h, l); (m) Statistic results of number fraction of ESCs in different regions; (n) Statistic results of area fraction of ESCs in different regions

increased fine equiaxed crystals. With increasing Mn content, the presence of ESCs escalates compared to the AM60 alloy. Conversely, adding trace RE elements (Ce and La) significantly reduces ESCs, transforming the distribution of refined grains from a linear to a small-area block-like pattern in the center and transition regions.

The statistical results of the number fraction of ESCs and the area fraction of ESCs in different regions are shown in Figs. 3(m) and (n), respectively. It is evident that, except for the center of AM61, the number fraction of ESCs in all regions of AM60-0.2Ce and AM60-0.2La alloys, as well as the transition and surface regions of AM61, is lower than that in AM60. Although the number fraction of ESCs in various regions of the four alloys accounts for no more than 4%, they occupy a significant area fraction of 6% to 45%, highlighting ESCs as a critical factor influencing the performance of the alloys.

3.2 Phase distribution

The XRD patterns of the studied HPDC alloys are illustrated in Fig. 4. The AM60 based alloys are mainly composed of α-Mg and $Mg_{17}Al_{12}$ phases. The diffraction peak intensities corresponding to the $Mg_{17}Al_{12}$ phase are uniformly low across all four alloys, with no significant differences observed. This suggests that adding Mn, Ce, and La elements has a negligible effect on the content of the $Mg_{17}Al_{12}$ phase in AM60 alloy.

Figure 5 illustrates SEM images of the AM60 based alloys at different magnifications. At higher magnifications, these images reveal the distribution of the secondary phase in the four alloys. The AM60 alloy exhibits a relatively low content of the secondary phase. Microalloying increases the secondary phase content, although the overall difference remains small. The increase in Mn content leads to a rise in the amount of spherical and irregular stripe phases. Microalloying of Ce and La significantly increases the volume fraction of the dispersed secondary phase at the grain boundaries. The AM60-0.2La alloy shows the highest content of the secondary phase.

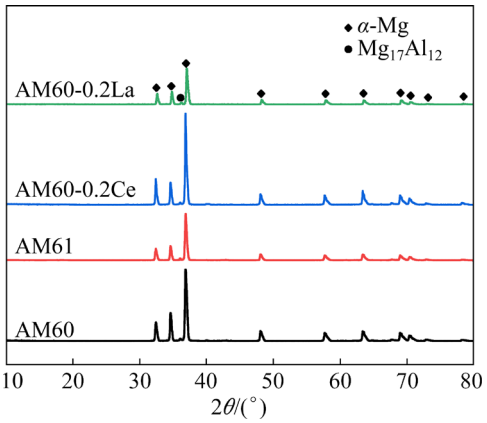

Fig. 4 XRD results of HPDC AM60 based alloys

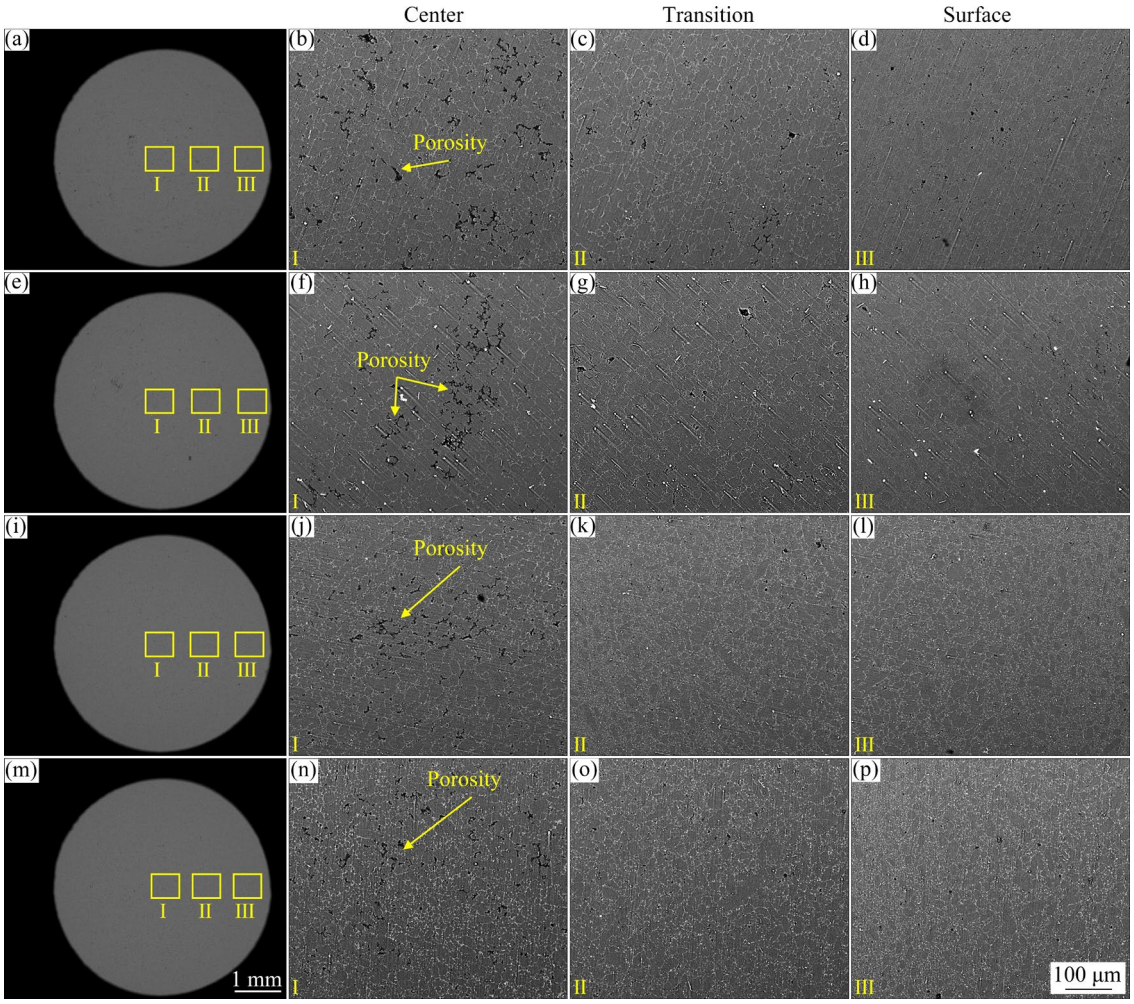

Fig. 5 SEM images of HPDC AM60 based alloys in different regions: (a−d) AM60; (e−h) AM61; (i−l) AM60-0.2Ce; (m−p) AM60-0.2La; (a, e, i, m) Overall SEM images; (b−d, f−h, g−l, n−p) Enlarged images of regions I, II, and III in (a, e, i, m), respectively

In addition, the generalized distribution of pores in the overall cross-section of the alloys is depicted in Figs. 5(a, e, i, m) at low magnifications. No distinct defect bands are evident in the four alloys, with defects predominantly concentrated in the center and decreasing towards the surface. The surface is almost free of defects. Combining SEM images at different magnifications reveals that the AM61 alloy exhibits the highest defect density in the center. The AM61 alloy shows more aggregated defects in the center, with individual defects occupying a significantly larger area than in the AM60 alloy. In contrast, the AM60-0.2Ce and AM60-0.2La alloys demonstrate a significant reduction in the number of defects compared to the AM60 alloy, with a notable decrease in pore size.

The AM60 and AM60-0.2La alloys were selected for the TEM analysis. Typical TEM images of irregularly shaped and massive phases in the AM60 samples are shown in Fig. 6. As depicted in Fig. 6(b), aluminum and manganese elements are uniformly distributed. Based on the high-angle annular dark field (HAADF) imaging, EDS energy spectrum (Fig. 6(b)), and the corresponding selected area electron diffraction (SAED) patterns (Figs. 6(c−h)), the irregularly shaped Mg−Al phase was confirmed to be $Mg_{17}Al_{12}$, with a body-centered cubic structure (lattice constant a=1.056 nm). The massive Al−Mn phases were identified as Al_8Mn_5, with a body-centered cubic structure (lattice constant a=0.901 nm).

Figure 7 illustrates typical TEM images of aggregated bar, globular, irregular elongated, and irregular spherical phases in AM60-0.2La samples, which exhibit significantly different morphologies compared to the AM60 alloy. Based on the HAADF plot (Fig. 7(f)), EDS maps (Fig. 7(g)), and the corresponding SAED patterns, the aggregated bar-like and globular phases in the AM60-0.2La alloy were identified as two different morphologies of the $Mg_{17}Al_{12}$ phase. The irregular elongated Al−La phase was identified as the $Al_{11}La_3$ phase, with a body-centered rhombohedral structure (lattice constants a=0.44 nm, b=1.01 nm, and c=1.31 nm). The irregular spherical Al−Mn−La phase was identified as the Al_8Mn_4La phase, with a body-centered tetragonal structure (lattice constants a=0.91 nm, and c=0.51 nm).

Compared to the AM60 alloy, the AM60-0.2La alloy displayed a change in the type of the secondary phase, with the absence of the Al_8Mn_5 phase and the appearance of the $Al_{11}La_3$ and Al_8Mn_4La phases. Notably, both Al_8Mn_4RE and $Al_{11}RE_3$ phases have high melting points, especially $Al_{11}RE_3$ phase, which has a melting point as high as 1240 °C, favoring improved YS and creep resistance [12].

3.3 Die-casting defects

Figure 8 illustrates the pore distribution and morphology via X-ray tomography. The CT images

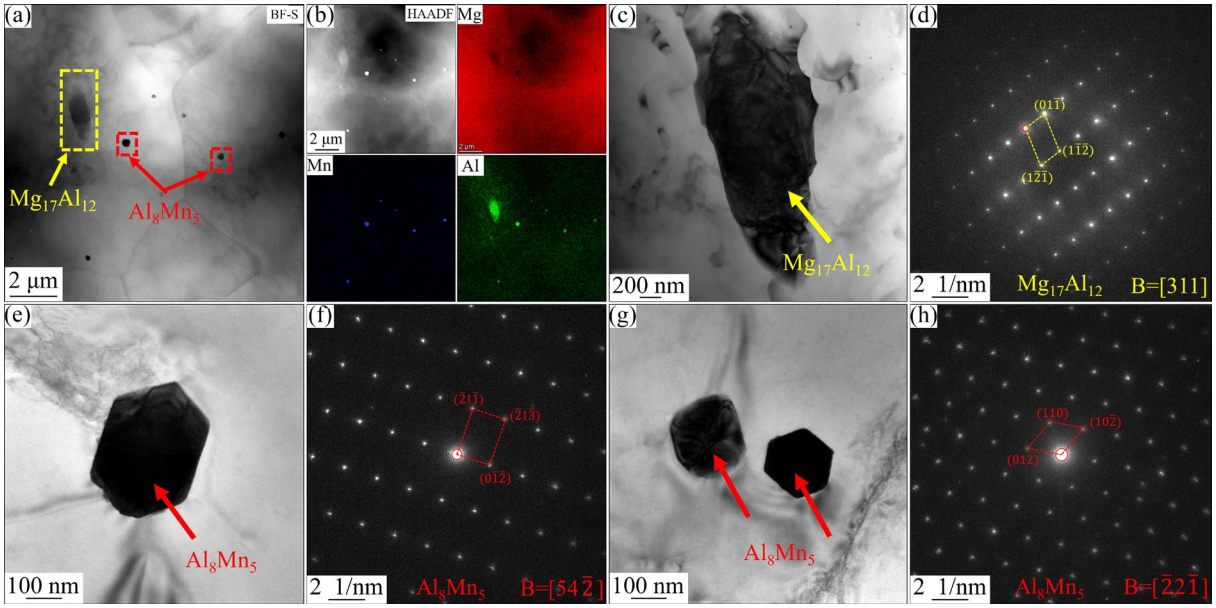

Fig. 6 TEM images of AM60 alloy: (a) BF-TEM image; (b) HAADF image and corresponding EDS spectra; BF-TEM images (c, e, g) and corresponding SAED patterns (d, f, h) for various secondary phases

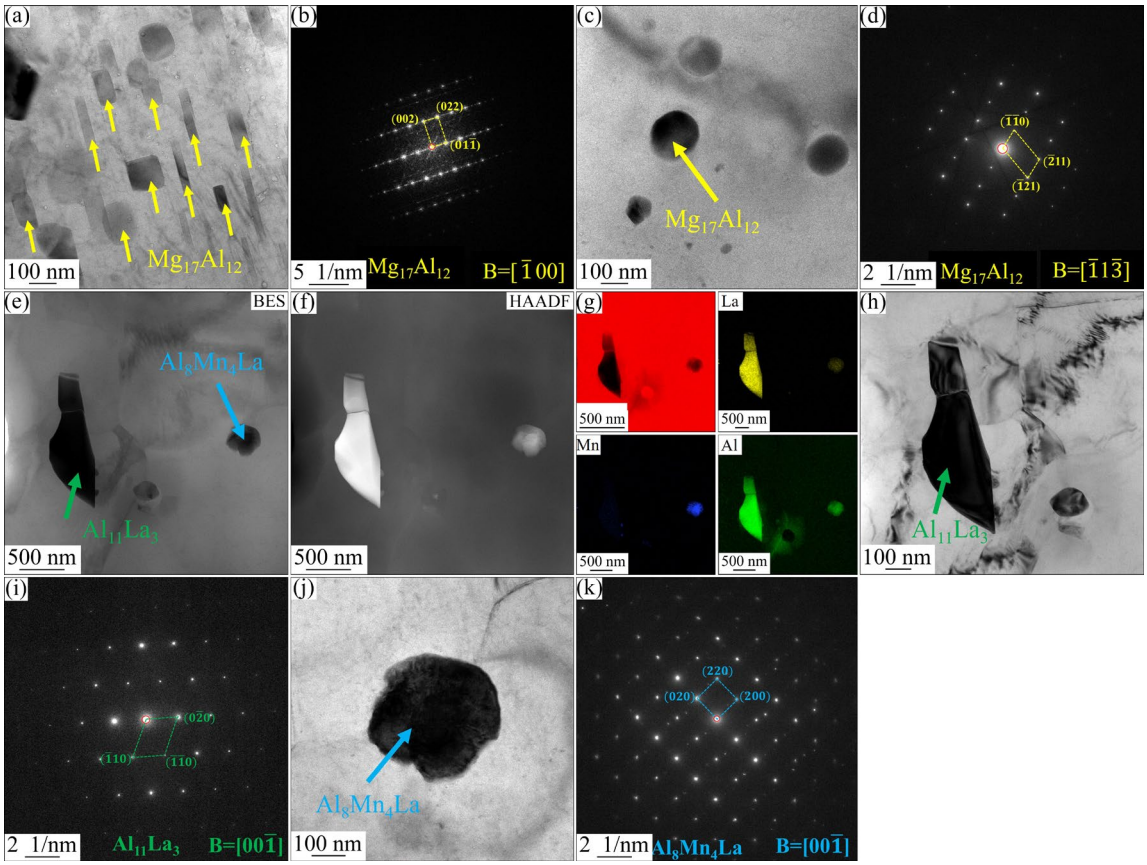

Fig. 7 TEM images of AM60-0.2La alloy: (a, c, h, j) BF-TEM images of secondary phases with distinct morphologies; (b, d, i, k) SAED patterns corresponding to (a, c, h, j), respectively; (e−g) Low-magnification BF-TEM micrograph (e) and HAADF image (f) and corresponding EDS map (g)

(Figs. 8(a, e, i, m)) reveal that the AM61 alloy exhibits the highest pore density, while the AM60-0.2La alloy displays the lowest pore density. Defects are concentrated in the center of the cross-section, diminishing toward the surface. Region I in the center contains numerous large and irregular pores, including air pores, air-contracted pores, net-contracted pores, island-contracted pores, and a mixed morphology. In the transition region II, the pore size gradually decreases, resulting in slightly more significant, aggregated, connected pores with complex morphologies. Small pores and island shrinkage porosity are observed near the surface in region III. These harmful defects are highly prone to evolving during the service life of the alloy, leading to the interconnection of defects. This results in the formation of larger defects, making the alloy more susceptible to failure.

Further analysis yields the pore distribution scatter diagram and the total porosity rate diagram for different alloys (Fig. 9(a)). AM61 exhibits the highest volume-equivalent sphere diameter (D_{ves}) and porosity, with a D_{ves} of 212 μm, indicating the presence of large pores. In comparison, the largest D_{ves} for AM60-0.2La is only 79 μm. The porosity rates for AM60, AM61, AM60-0.2Ce, and AM60-0.2La are 0.030%, 0.057%, 0.015%, and 0.006%, respectively. The number and area fractions of large pores with a D_{ves} over 65 μm (pores with a volume > 135000 μm^3) are also counted and presented in Fig. 9(b). AM61 has the highest number of large pores, whereas the addition of 0.2 wt.% La results in the fewest large pores.

3.4 Mechanical properties

Figure 10 presents the tensile engineering stress−strain curves of the AM60 based die-casting alloys. Table 2 shows the UTS, YS, and EL at RT. The AM60 alloy exhibits a YS of (152±1.0) MPa, a UTS of (280.3±1.5) MPa, and an EL of (19.9±0.8)%. The content of Mn was incrementally adjusted from 0.31 wt.% to 0.59 wt.%, leading to a slight decrease in both the YS and UTS, whereas a notable increase was observed in the EL. This phenomenon might be

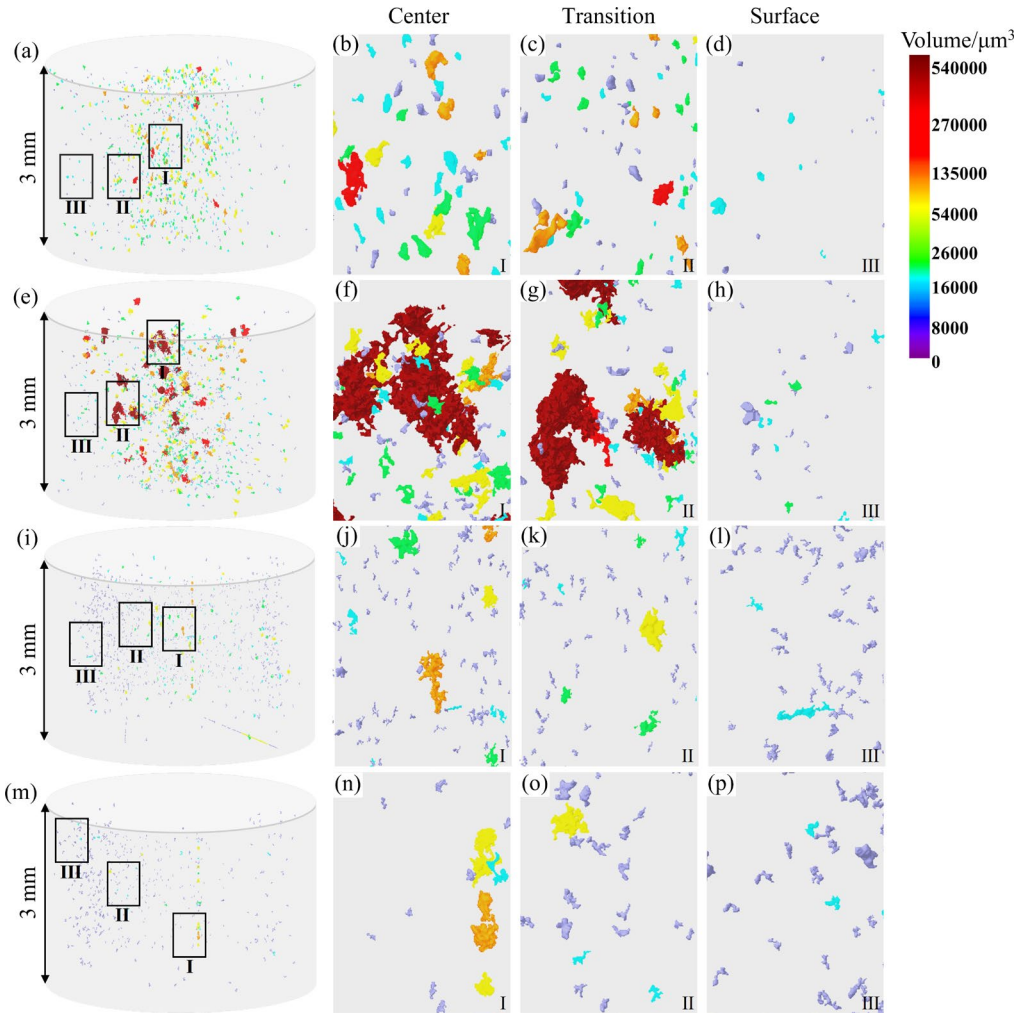

Fig. 8 3D reconstructed images of HPDC AM60 based alloys: (a−d) AM60; (e−h) AM61; (i−l) AM60-0.2Ce; (m−p) AM60-0.2La; (a, e, i, m) Overall 3D images; (b−d, f−h, j−l, n−p) Enlarged views of regions I, II, and III in (a, e, i, m), respectively

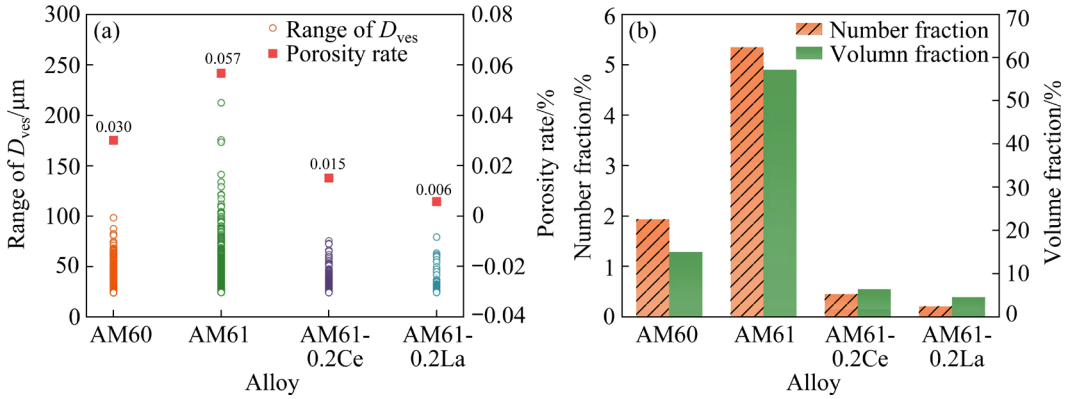

Fig. 9 (a) Scatter diagram of pore distribution and porosity rate in HPDC AM60 based alloys; (b) Comparison diagram of number fraction and volume fraction of pores with D_{ves}>65 μm (V>135000 μm³)

attributed to variations in the internal porosity density of the alloy. Notably, the mechanical properties of AM60-0.2Ce and AM60 alloys exhibit remarkable similarity. The introduction of La as a microalloying element significantly enhanced the comprehensive mechanical performance of the AM60

alloy under the experimental conditions in this study. Specifically, the AM60-0.2La alloy achieved the UTS, YS, and EL of (288.0±1.7) MPa, (158.0±1.0) MPa, and (22.0±3.0)%, respectively. These alloys demonstrate a superior combination of strength and plasticity compared to other commercial alloys such as AZ91D, AM40, and AE44 [13−15]. Among commercial and newly developed HPDC magnesium alloys, the studied alloys exhibit the highest mechanical properties, as shown in Fig. 10(b).

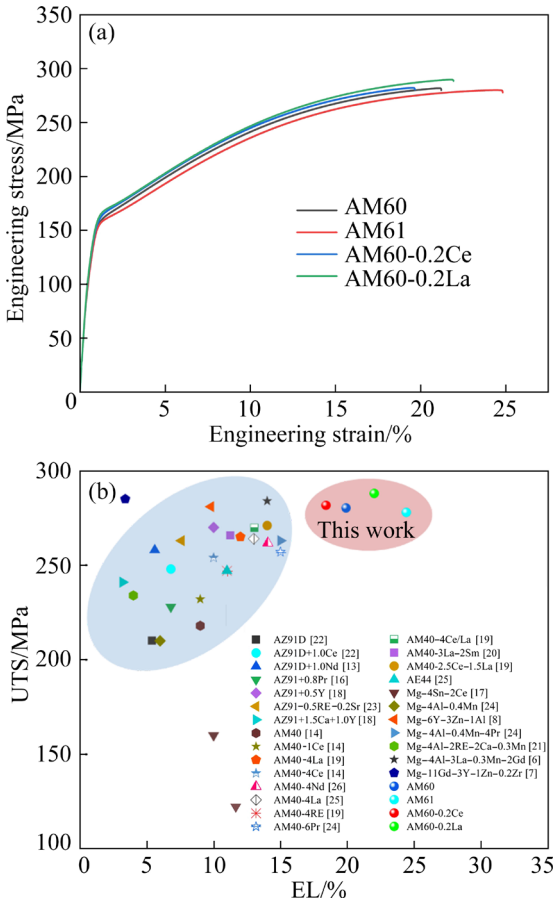

Fig. 10 (a) Tensile curves and corresponding mechanical properties of HPDC AM60 based alloys; (b) UTS and EL of various HPDC Mg alloys in this work and from Refs. [6−8,13,14,16−26]

Table 2 Mechanical properties of HPDC AM60 based alloys

Alloy	UTS/MPa	YS/MPa	EL/%
AM60	280.3±1.5	152.0±1.0	19.9±0.8
AM61	278.0±2.6	148.3±1.5	24.4±1.6
AM60-0.2Ce	281.7±0.6	158.0±2.4	18.4±0.7
AM60-0.2La	288.0±1.7	158.0±1.0	22.0±3.0

Additionally, Fig. 11 reveals an abundance of ESCs in the center region of the cross-section, predominantly exhibiting cleavage fractures. Dimples with a few cleavage planes primarily characterize the transition region. The surface region displays refined grains, presenting a relatively smooth fracture surface with a ductile fracture pattern characterized by dimples. This characteristic is also observed in AZ91-Y based die-casting alloys [27]. Small dimples result from grain boundary cracks caused by stress transfer along the grain boundaries, known as transgranular fracture (ductile fracture). The cleavage steps indicate crack propagation of intermetallic compounds along the grain boundaries, referred to as intergranular fracture (brittle fracture). Therefore, the fracture patterns among different alloys show minimal variation, suggesting that the failure mode of the alloys is a mixture of ductile and brittle fractures.

3.5 Corrosion properties

Figure 12 depicts the corrosion properties of HPDC AM60 based alloys immersed in 3.5 wt.% NaCl solution for 168 h. The corrosion rate in the initial 36 h of immersion is slow. The cumulative hydrogen evolution volume for AM60, AM61, AM60-0.2Ce, and AM60-0.2La is 1.26, 2.65, 0.78, and 0.76 mL/cm^2, respectively, with AM60-0.2La exhibiting the lowest hydrogen evolution volume. The calculated hydrogen evolution rate increases from 0.48 mm/a for AM60 to 0.86 mm/a for AM61 but decreases to 0.31 and 0.29 mm/a with the addition of Ce and La, respectively. The corrosion rate of the AM60-0.2La alloy is marginally lower than that of high-purity magnesium (0.3 mm/a) [28], indicating superior corrosion resistance. Compared to the stainless magnesium alloy Mg−11Y−1Al (0.17 mm/a in 3.5 wt.% NaCl solution) developed by Shanghai Jiao Tong University, China [29], the performance difference of AM60-0.2La is not substantial, demonstrating its competitive corrosion resistance.

3.6 Fluidity

The fluidity of alloy melts is a crucial factor determining the castability of die-casting magnesium alloys [30]. Generally, superior fluidity enhances the capability to heal the hot tears and pores induced by solidification shrinkage, producing castings with reduced hot tearing susceptibility [31]. The fluidity

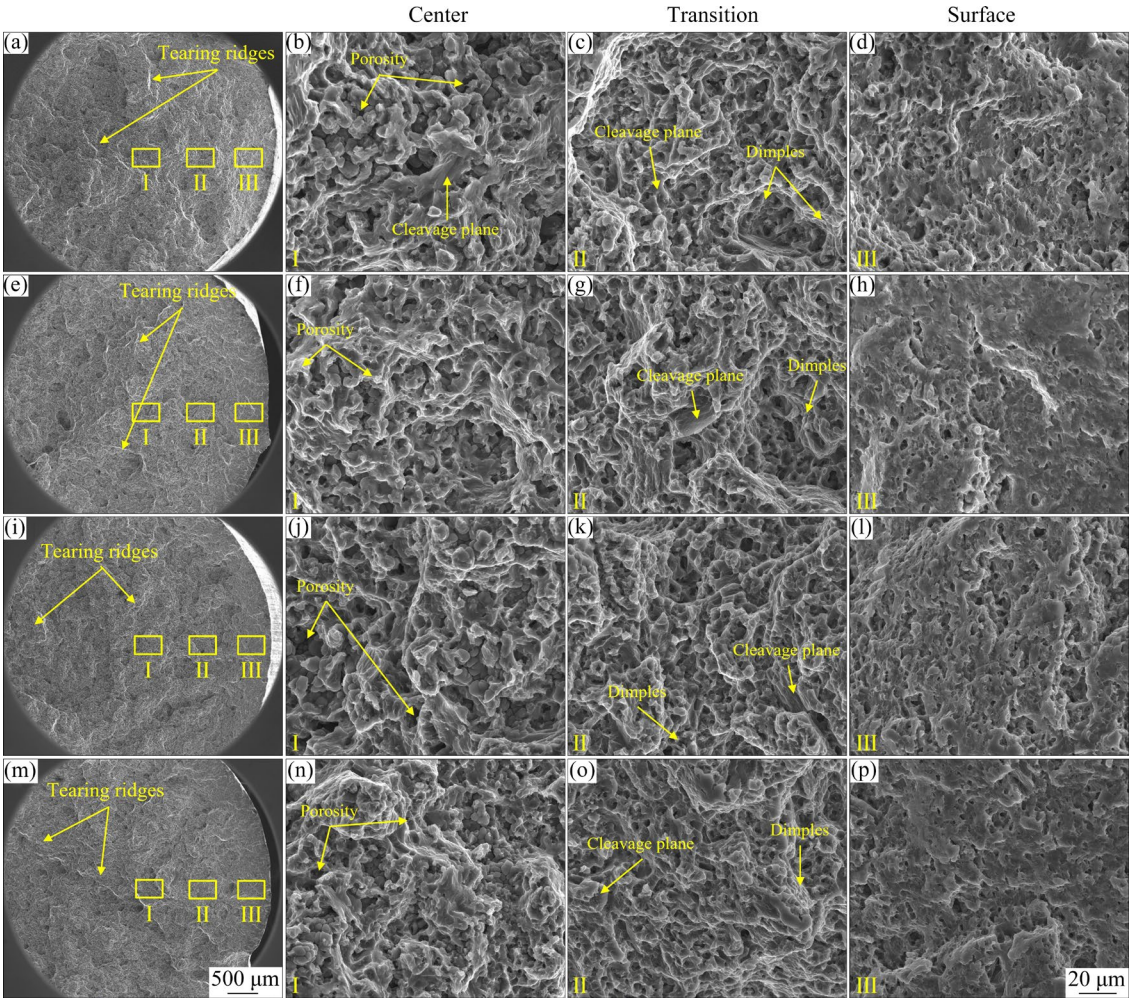

Fig. 11 SEM images of cross-sections of HPDC AM60 based alloys after tensile fracture: (a−d) AM60; (e−h) AM61; (i−l) AM60-0.2Ce; (m−p) AM60-0.2La; (a, e, i, m) Overall fracture morphologies; (b−d, f−h, j−l, n−p) Enlarged images of regions I, II, and III corresponding to (a, e, i, m), respectively

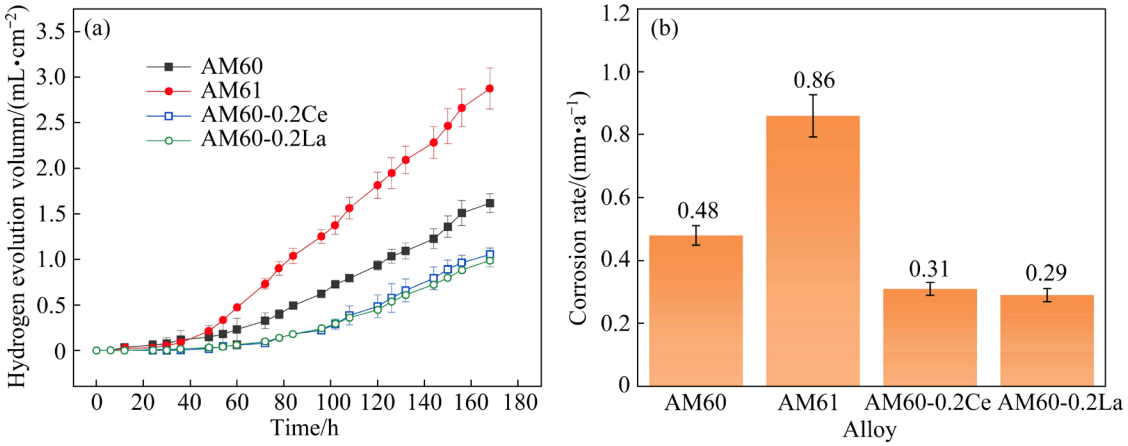

Fig. 12 Corrosion behavior of HPDC AM60 based alloys immersed in 3.5 wt.% NaCl solution for 168 h: (a) Hydrogen evolution volume−time curves; (b) Corrosion rate bar chart

of the four alloys was also investigated, and the results are shown in Fig. 13. The decreasing trend in fluidity among the four alloys is AM60-0.2La > AM60-0.2Ce > AM60 > AM61. It is obvious, that incorporating trace amounts of La significantly enhances the fluidity of the AM60 alloy by 74%. Conversely, increasing Mn content slightly decreases the flow length of the AM60 alloy. This may be one

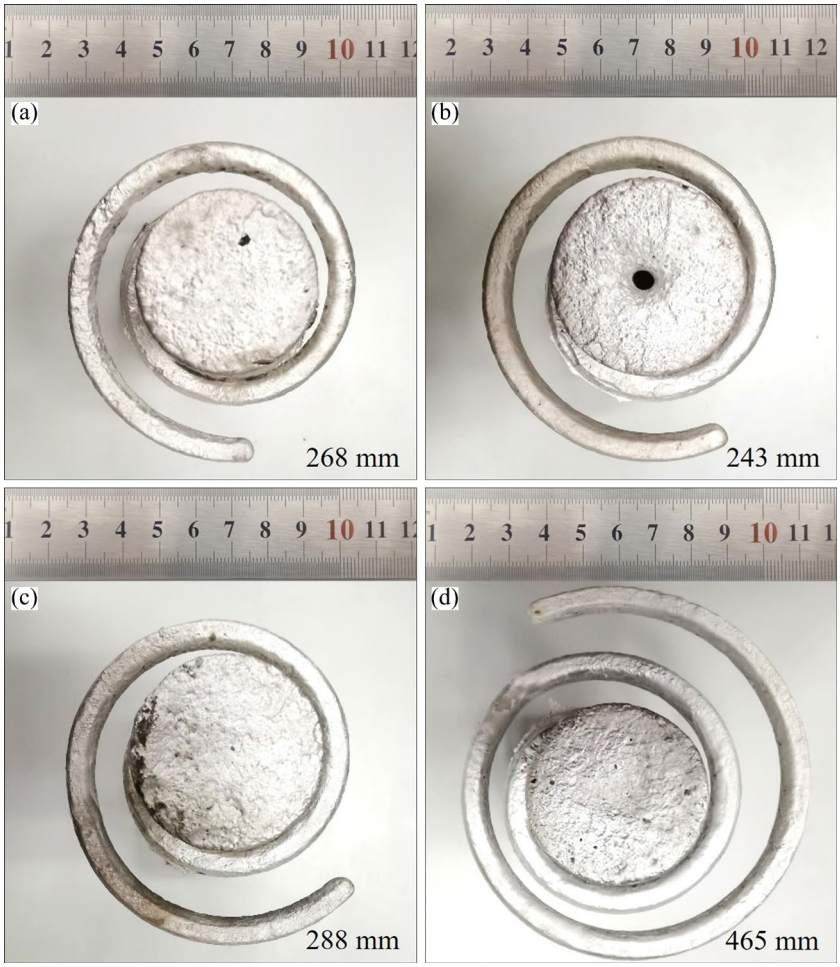

Fig. 13 Macro-view photographs of HPDC AM60 based alloys in fluidity test: (a) AM60; (b) AM61; (c) AM60-0.2Ce; (d) AM60-0.2La

of the reasons for the high defect density in AM61 alloy, leading to low performance and weak corrosion resistance.

4 Discussion

4.1 Effect of alloying on mechanical properties

The mechanical properties of HPDC magnesium alloys depend primarily on the grain size, secondary phase constituents, and defects (such as ESCs and porosity). In the case of die-casting magnesium alloy, the primary strengthening mechanisms involve solid solution strengthening, secondary phase strengthening, and grain refinement strengthening. Given the minor amounts of Mn, Ce, and La added in this study, the contributions of solid solution strengthening and secondary phase strengthening are considered negligible.

4.1.1 Grain refinement

According to the Hall−Petch relationship [32], the grain refinement significantly enhances the strength of alloys, particularly the YS. In addition, it serves as an effective method to enhance the ductility. The AGS (the average grain size in center, transition, and surface regions) of AM60 alloy is ~20.8 μm, while those of AM61, AM60-0.2Ce, and AM60-0.2La alloys are ~22.6, ~14.6, and ~15.9 μm, respectively. The addition of Ce and La led to the grain refinement in three regions. Compared to numerous alloys in Fig. 10(b), the AM60 based alloys developed in this study exhibit satisfactory grain refinement.

The fine grain primarily stems from solute atoms and the secondary phase of the alloy. Solute elemental segregation promotes additional nucleation, inhibiting the grain growth, a phenomenon termed compositional supercooling. The direct contribution of compositional supercooling induced by Mn to the grain refinement may be somewhat limited [33]. This may be why AM61

alloy only has grain refinement in the surface region and excessive areas. The grain refinement observed in AM60-0.2Ce and AM60-0.2La alloys is primarily attributed to compositional supercooling of the solute atoms [34] and grain confinement of the $Al_{11}RE_3$ phase due to the synergistic refining effect of heterogeneous nucleation [35].

4.1.2 Die-casting defects

The HPDC process, characterized by slow pressure injection, fast filling, and rapid cooling, often causes defects such as pre-crystallization, porosity, and shrinkage, which negatively impact the mechanical properties of the parts [36].

The fluidity of die-casting alloys significantly influences the formation of ESCs by affecting solidification time. Increasing Mn content decreases the alloy fluidity, prolongs flow time during injection, and promotes larger ESCs. Figure 3(m) illustrates that the center of the AM61 alloy has a higher number fraction of ESCs compared to the AM60 alloy, with ESCs occupying the largest area fraction. Moreover, shorter injection flow time decreases the formation probability and size of the ESCs.

The aggregation of ESCs influences pore formation: fewer ESCs lead to smaller-sized pores or island-like shrinkage, while a greater number of ESCs result in larger-sized mesh or island-like shrinkage. Numerous studies [37−39] have demonstrated that the strength and elongation of HPDC magnesium alloys are related to the pore volume fraction. LI et al [37] reported that irregularly shaped shrinkage, including net and air shrinkage, is the primary source of crack initiation, significantly detrimental to the mechanical properties of castings. Similarly, ZHANG et al [40] found that the largest pore in HPDC alloys has the most detrimental impact on the mechanical properties.

Sphericity differentiates pore types, with a value between 0 and 1, where 1 indicates a perfect sphericity. Figure 14 presents the sphericity statistics for all pores in the four alloys based on Micro-CT data, revealing significant differences in pore sphericity among the four alloys. Compared to the AM60 alloy, the pore sphericity decreases with increasing the Mn content and the addition of rare earth elements, with the size ranking AM60 > AM61 > AM60-0.2La > AM60-0.2Ce.

Figures 15(a−d) show the scatter plots of sphericity versus D_{ves} of defects in the four AM60 based alloys. Defects with sphericity less than 0.6 are

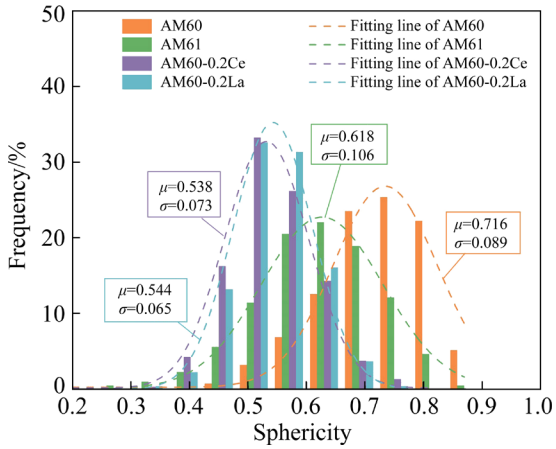

Fig. 14 Sphericity statistics of pores of HPDC AM60 based alloys (μ is average sphericity; σ is standard deviation of sphericity)

shrinkage porosity; those with sphericity greater than 0.6 are stagnant air entrapment. AM60 alloy has many air entrapments, while AM61 alloy shows reduced entrapments but increased shrinkage porosity. AM60-0.2Ce and AM60-0.2La alloys significantly reduce entrapments and the D_{ves} of low-sphericity shrinkage porosity compared to AM60, with AM60-0.2La being more effective. This study reveals that shrinkage porosity negatively impacts mechanical properties of HPDC alloys more greatly than high sphericity pores.

Figures 15(e−h) show the 3D morphologies of the most prominent pores in the four AM60 based alloys from Micro-CT data. The AM61 alloy has the largest pore with the D_{ves} of 212.43 μm and the lowest sphericity, making it more hazardous to mechanical properties than AM60. In contrast, the maximum D_{ves} values of AM60-0.2Ce and AM60-0.2La alloys are significantly reduced. Despite AM60-0.2La having a larger maximum D_{ves} than AM60-0.2Ce, it has fewer and smaller volume fraction of pores larger than 65 μm in Fig. 9, decreasing crack initiation likelihood. Thus, defects in AM60-0.2La are the least detrimental to mechanical properties.

4.2 Effect of alloying on corrosion properties

For magnesium alloys, the impurity content, grain size, secondary phases, and defects are key factors affecting corrosion behavior. The decreasing corrosion resistance of the four alloys is as follows: AM60-0.2La > AM60-0.2Ce > AM60 > AM61.

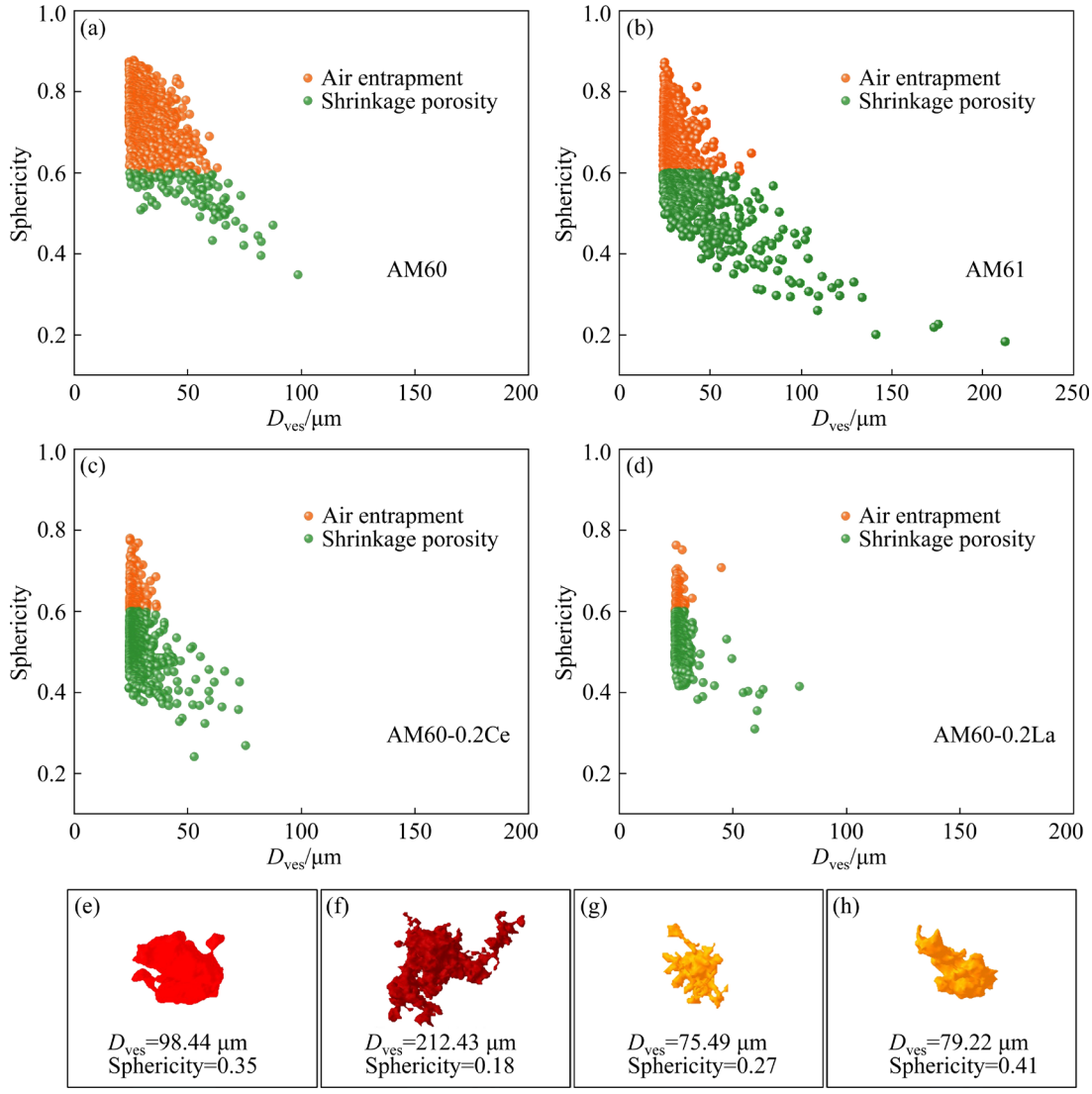

Fig. 15 Relationship between sphericity and D_{ves} of defects (a−d) and 3D morphologies of largest pore (e−h) in HPDC AM60 based alloys: (a, e) AM60; (b, f) AM61; (c, g) AM60-0.2Ce; (d, h) AM60-0.2La

4.2.1 Impurity content

During the melting process, magnesium alloys tend to generate non-metallic inclusions, with impurity elements, notably Fe, posing a substantial threat to their corrosion resistance [41]. Research indicates that increasing the Mn content can effectively mitigate Fe content. Adding RE elements can reduce the inclusion content [42], thereby enhancing the purification of the magnesium melt and subsequently improving corrosion resistance [43]. Therefore, adding Mn, La, and Ce will decrease the corrosion rate of AM60 alloy.

4.2.2 Secondary phase

The contents of the secondary phases ($Mg_{17}Al_{12}$ and $Al_{11}RE_3$) in the four AM60 based alloys are calculated by Pandat software, as listed in Table 3. The addition of Mn does not alter the composition of the secondary phase in the alloy and slightly reduces the content of $Mg_{17}Al_{12}$. The addition of RE elements Ce and La is helpful for precipitating the $Al_{11}RE_3$ intermetallic phase and inhibiting the precipitation of the $Mg_{17}Al_{12}$ phase [44], with La having a more pronounced effect.

Table 3 Contents of $Mg_{17}Al_{12}$ and $Al_{11}RE_3$ phases in four AM60 based alloys (wt.%)

Alloy	$Mg_{17}Al_{12}$	$Al_{11}RE_3$
AM60	0.684899	–
AM61	0.684897	–
AM60-0.2Ce	0.684765	0.000126
AM60-0.2La	0.684574	0.000198

The corrosion behavior is related to the electrode potential difference between different phases, which can lead to different degrees of galvanic coupling corrosion. This corrosion occurs due to varying potential differences between the secondary phase of different compositions and the magnesium matrix [45].

Incorporating RE elements Ce and La results in the precipitation of the $Al_{11}RE_3$ phase while suppressing the formation of the $Mg_{17}Al_{12}$ phase. In a study by LIU et al [46], the potential of the $Mg_{17}Al_{12}$ phase is 26 mV lower than that of the α-Mg phase, whereas the potential of the $Al_{11}RE_3$ phase is only 8 mV lower than that of the α-Mg phase. Consequently, the $Al_{11}RE_3$ phase will decrease the micro-galvanic corrosion of magnesium alloy, similar to the corrosion law found by GALICIA et al [47]. Additionally, RE elements facilitate the generation of Al−RE oxides and hydroxides, thereby densifying the corrosion products of AM60-RE alloy and enhancing its protective capacity [48]. Hence, the addition of La and Ce will decrease the corrosion rate of AM60 alloy.

4.2.3 Defects

For die-casting magnesium alloys, casting defects such as shrinkage and porosity significantly impact the corrosion performance. Corrosion typically initiates at these casting defects and intensifies over time, spreading throughout the matrix. AM61 alloy exhibits more casting defects than AM60 alloy, increasing the actual surface area of the sample and leading to more pronounced directional corrosion. In contrast, AM60-0.2Ce and AM60-0.2La alloys have significantly reduced casting defects, enhancing their corrosion resistance. Therefore, adding Mn to AM60 alloy substantially increases its corrosion rate, while adding La and Ce decreases it.

4.3 Effect of alloying on fluidity

The decreasing fluidity order of the four alloys is as follows: AM60-0.2La > AM60-0.2Ce > AM60 > AM61. This variation in fluidity can be attributed to two primary factors. Firstly, the content of the Al_8Mn_5 phase before the precipitation of α-Mg phase in AM60 based alloys was calculated by Pandat software (Table 4). The higher Mn content in AM61 leads to the increased Al_8Mn_5 phase, whereas the minor additions of Ce and La decrease its content. The precipitation of phases like Al_8Mn_5 before α-Mg increases the melt viscosity, thus reducing fluidity [49,50]. Secondly, the diffusion coefficients [51,52] of elements in Mg melt, following the decreasing order of La > Ce > Al > Mn, contribute to higher fluidity due to faster diffusion rates.

Table 4 Al_8Mn_5 phase content before α-Mg phase precipitation in AM60 based alloys

Alloy	Al_8Mn_5 phase content/wt.%
AM60	1.50×10^{-6}
AM61	1.84×10^{-6}
AM60-0.2Ce	3.08×10^{-7}
AM60-0.2La	2.15×10^{-7}

5 Conclusions

(1) The microstructures of AM60 based die-casting alloys mainly comprise larger ESCs and fine equiaxed crystals. The addition of Mn, Ce, and La reduces the grain size of AM60 alloy. However, in AM61 alloy, ESCs have the highest proportion. The decreasing order of alloy porosity rate is as follows: AM61 > AM60 > AM60-0.2Ce > AM60-0.2La.

(2) The room temperature tensile test results of the four AM60 based alloys demonstrate an excellent balance between strength and plasticity. The strengthening methods are mainly fine crystal strengthening, and defects such as pre-crystallization and large porosity damage the strength and plasticity of the alloy. AM60-0.2La alloy exhibits the optimal mechanical performance, with a UTS of (288.0±1.7) MPa, a YS of (158.0±1.0) MPa, and an EL of (22.0±3.0)%.

(3) The corrosion resistance of the four AM60 based alloys from high to low is ranked as follows: AM60-0.2La > AM60-0.2Ce > AM60 > AM61. AM60-0.2La exhibits the best corrosion resistance, with a corrosion rate of 0.29 mm/a, approximately 40% lower than that of the AM60 alloy. It can be attributed to the purification effect of La on the magnesium melt, the precipitation of the $Al_{11}RE_3$ phase with a low potential difference, and the achievement of the lowest porosity.

(4) The fluidity of the alloys from high to low is ranked as follows: AM60-0.2La > AM60-0.2Ce > AM60 > AM61. The incorporation of Mn, Ce, and La elements impacts the quantity of the preferentially precipitated Al_8Mn_5 phase, thus affecting the fluidity. Furthermore, the variation in

diffusion coefficients of elements in the magnesium melt contributes to the difference in fluidity observed among AM60-based alloys.

CRediT authorship contribution statement

Jing WANG: Conceptualization, Data curation, Formal analysis, Investigation, Writing − Original draft; **Xin GUO:** Conceptualization, Data curation, Formal analysis, Software, Investigation, Writing − Original draft, Review & editing; **Jiang-feng SONG:** Conceptualization, Funding acquisition, Project administration, Supervision, Writing − Review & editing; **Dang-he SHI:** Methodology, Supervision, Writing − Review & editing; **He-cong XIE:** Methodology, Investigation, Writing − Review & editing; **Chun-yu LI:** Methodology, Formal analysis, Writing − Review & editing; **Heng-rui HU:** Software, Writing − Review & editing; **Gong CHEN:** Methodology, Writing − Review & editing; **Bin JIANG:** Conceptualization, Funding acquisition, Project administration, Resources, Writing − Review & editing; **Dong-xia XIANG:** Supervision; **Fu-sheng PAN:** Funding acquisition, Project administration, Resources, Writing − Review & editing.

Declaration of competing interest

The authors declare that they have no known competing financial interests or personal relationships that could have appeared to influence the work reported in this paper.

Acknowledgments

This work was financially supported by the National Key Research and Development Program of China (Nos. 2022YFB3709300, 2021YFB3701000), the National Natural Science Foundation of China (Nos. 52271090, 52071036, U2037601, U21A2048), Chongqing Science and Technology Commission, China (Nos. CSTB2022TIAD-KPX0021, CSTC2024YCJH-BGZXM0164, CSTB2024TIAD-KPX0001), and the Fundamental Research Funds for the Central Universities, China (No. 2022CDJDX-002).

References

[1] LIU Zhan, NIE Jin-feng, ZHAO Yong-hao. Effect of deformation processing on microstructure evolution and mechanical properties of Mg−Li alloys: A review [J]. Transactions of Nonferrous Metals Society of China, 2024, 34: 1−25.

[2] PATEL V, WOUTERS H, BAGHDADCHI A, de BACKER J, IGESTRAND M, AZIMI S, ANDERSSON J. Robotic friction stir welding in lightweight battery assembly of extrusion-cast aluminium alloys [J]. Journal of Advanced Joining Processes, 2023, 8: 100156.

[3] LI Tian, SONG Jiang-feng, ZHANG Ang, YOU Guo-qiang, YANG Yan, JIANG Bin, QIN Xian-yue, XU Cheng, PAN Fu-sheng. Progress and prospects in Mg-alloy super-sized high pressure die casting for automotive structural components [J]. Journal of Magnesium and Alloys, 2023, 11: 4166−4180.

[4] THANABAL N, SILAMBARASAN R, SEENUV-ASAPERUMAL P, BASHA D A, ELAYAPERUMAL A. Microstructure and mechanical behavior of AXM Mg alloy systems—A review [J]. Journal of Magnesium and Alloys, 2024, 12: 2624−2646.

[5] ZHANG Jing-huai, ZHANG Mi-lin, MENG Jian, WU Rui-zhi, TANG Ding-xiang. Microstructures and mechanical properties of heat-resistant high-pressure die-cast Mg−4Al−*x*La−0.3Mn (*x*=1, 2, 4, 6) alloys [J]. Materials Science and Engineering: A, 2010, 527: 2527−2537.

[6] LV Shu-hui, LÜ Xiao-ling, MENG Fan-zhi, YANG Qiang, QIU Xin, QIN Peng-fei, DUAN Qian, MENG Jian. Microstructures and mechanical properties in a Gd-modified high-pressure die casting Mg−4Al−3La−0.3Mn alloy [J]. Materials Science and Engineering: A, 2020, 773: 138725.

[7] CHANG Zhi-yu, DENG Qing-chen, LAN Qiao, FENG Jian, LI Da-quan, LIU Bao-liang, WU Yu-juan, PENG Li-ming, DING Wen-jiang. Microstructure and mechanical properties of Mg−Gd−Y−Zn−Zr alloy prepared by rheo-diecasting [J]. Materials Science and Engineering: A, 2022, 848: 143287.

[8] BAI Yang, YE Bing, WANG Li-yang, ZHAO Bei-bei, YU Xin, LU Yong, KONG Xiang-yang, DING Wen-jiang. A novel die-casting Mg alloy with superior performance: Study of microstructure and mechanical behavior [J]. Materials Science and Engineering: A, 2021, 802: 140655.

[9] LI Sheng-yong, LI De-jiang, ZENG Xiao-qin, DING Wen-jiang. Microstructure and mechanical properties of Mg−6Gd−3Y−0.5Zr alloy processed by high-vacuum die-casting [J]. Transactions of Nonferrous Metals Society of China, 2014, 24: 3769−3776.

[10] SUN Yue-hua, ZHANG Fan, YANG Bin, REN Jian, SONG Guang-sheng. Effect of extrusion ratio on microstructure, texture, and mechanical properties of dual-phase Mg−8Li−6Zn−2Gd alloy [J]. Transactions of Nonferrous Metals Society of China, 2024, 34: 833−845.

[11] CAO Fu-yong, SHI Zhi-ming, HOFSTETTER J, UGGOWITZER P J, SONG Guang-ling, LIU Ming, ATRENS A. Corrosion of ultra-high-purity Mg in 3.5% NaCl solution saturated with $Mg(OH)_2$ [J]. Corrosion Science, 2013, 75: 78−99.

[12] EFTEKHAR A H, SADROSSADAT S M, REIHANIAN M. Microstructural investigation and high temperature mechanical behavior of AXE622 cast Mg alloy [J]. Metals and Materials International, 2022, 28: 1062−1074.

[13] YANG You, LI Xue-song. Influence of neodymium on high cycle fatigue behavior of die cast AZ91D magnesium alloy [J]. Journal of Rare Earths, 2010, 28: 456−460.

[14] ZHANG Jing-huai, LENG Zhe, ZHANG Mi-lin, MENG Jian, WU Rui-zhi. Effect of Ce on microstructure, mechanical properties and corrosion behavior of high-pressure die-cast

Mg−4Al-based alloy [J]. Journal of Alloys and Compounds, 2011, 509: 1069−1078.

[15] LI X, XIONG S M, GUO Z P. Improved mechanical properties in vacuum-assist high-pressure die casting of AZ91D alloy [J]. Journal of Materials Processing Technology, 2016, 231: 1−7.

[16] CUI Xiao-peng, LIU Hai-feng, MENG Jian, ZHANG De-ping. Microstructure and mechanical properties of die-cast AZ91D magnesium alloy by Pr additions [J]. Transactions of Nonferrous Metals Society of China, 2010, 20: 435−438.

[17] ÖZARSLAN S, ŞEVIK H, SORAR İ. Microstructure, mechanical and corrosion properties of novel Mg−Sn−Ce alloys produced by high pressure die casting [J]. Materials Science and Engineering: C, 2019, 105: 110064.

[18] WANG Feng, WANG Yue, MAO Ping-li, YU Bao-yi, GUO Quan-ying. Effects of combined addition of Y and Ca on microstructure and mechanical properties of die casting AZ91 alloy [J]. Transactions of Nonferrous Metals Society of China, 2010, 20: 311−317.

[19] XIE Jin-shu, ZHANG Jing-huai, YOU Zi-hao, LIU Shu-juan, GUAN Kai, WU Rui-zhi, WANG Jun, FENG Jing. Towards developing Mg alloys with simultaneously improved strength and corrosion resistance via RE alloying [J]. Journal of Magnesium and Alloys, 2021, 9: 41−56.

[20] YANG Qiang, BU Fan-qiang, MENG Fan-zhi, QIU Xin, ZHANG De-ping, ZHENG Tian, LIU Xiao-juan, MENG Jian. The improved effects by the combinative addition of lanthanum and samarium on the microstructures and the tensile properties of high-pressure die-cast Mg−4Al-based alloy [J]. Materials Science and Engineering: A, 2015, 628: 319−326.

[21] YANG Qiang, GUAN Kai, BU Fan-qiang, ZHANG Ya-qin, QIU Xin, ZHENG Tian, LIU Xiao-juan, MENG Jian. Microstructures and tensile properties of a high-strength die-cast Mg−4Al−2RE−2Ca−0.3Mn alloy [J]. Materials Characterization, 2016, 113: 180−188.

[22] YANG You, LIU Yong-bing, QIN Shu-ying, FANG Yi. High cycle fatigue properties of die-cast magnesium alloy AZ91D with addition of different concentrations of cerium [J]. Journal of Rare Earths, 2006, 24: 591−595.

[23] ZHANG Dong-dong, ZHANG De-ping, BU Fan-qiang, LI Xin-lin, GUAN Kai, YANG Qiang, LIU Shao-hua, LIU Xiao-juan, MENG Jian. Effects of minor Sr addition on the microstructure, mechanical properties and creep behavior of high pressure die casting AZ91-0.5RE based alloy [J]. Materials Science and Engineering: A, 2017, 693: 51−59.

[24] ZHANG Jing-huai, LIU Ke, FANG Da-qing, QIU Xin, YU Peng, TANG Ding-xiang, MENG Jian. Microstructures, mechanical properties and corrosion behavior of high-pressure die-cast Mg−4Al−0.4Mn−xPr (x=1, 2, 4, 6) alloys [J]. Journal of Alloys and Compounds, 2009, 480: 810−819.

[25] ZHANG Jing-huai, YU Peng, LIU Ke, FANG Da-qing, TANG Ding-xiang, MENG Jian. Effect of substituting cerium-rich mischmetal with lanthanum on microstructure and mechanical properties of die-cast Mg−Al−RE alloys [J]. Materials & Design, 2009, 30: 2372−2378.

[26] ZHANG Jing-huai, WANG Jun, QIU Xin, ZHANG De-ping, TIAN Zheng, NIU Xiao-dong, TANG Ding-xiang, MENG Jian. Effect of Nd on the microstructure, mechanical properties and corrosion behavior of die-cast Mg−4Al-based alloy [J]. Journal of Alloys and Compounds, 2008, 464: 556−564.

[27] ZHANG Jing-huai, NIU Xiao-dong, QIU Xin, LIU Ke, NAN Chang-ming, TANG Ding-xiang, MENG Jian. Effect of yttrium-rich misch metal on the microstructures, mechanical properties and corrosion behavior of die cast AZ91 alloy [J]. Journal of Alloys and Compounds, 2009, 471: 322−330.

[28] ATRENS A, SHI Zhi-ming, MEHREEN S U, JOHNSTON S, SONG Guang-ling, CHEN Xian-hua, PAN Fu-sheng. Review of Mg alloy corrosion rates [J]. Journal of Magnesium and Alloys, 2020, 8: 989−998.

[29] ZHU Qing-chun, LI Yang-xin, CAO Fu-yong, QIU Dong, YANG Yao, WANG Jing-ya, ZHANG Huan, YING Tao, DING Wen-jiang, ZENG Xiao-qin. Towards development of a high-strength stainless Mg alloy with Al-assisted growth of passive film [J]. Nature Communications, 2022, 13: 5838.

[30] SHEVIDI A H, TAGHIABADI R, RAZAGHIAN A. Weibull analysis of effect of T6 heat treatment on fracture strength of AM60B magnesium alloy [J]. Transactions of Nonferrous Metals Society of China, 2018, 28: 20−29.

[31] GUO Xin, ZHAO Hua, SONG Jiang-feng, JIANG Bin, XIE Wen-long, LIAO Jin-ge, XIE He-cong, WANG Jing, XIAO Jian-fei, PAN Fu-sheng. Effect of Ca on hot tearing susceptibility of WE43 alloy [J]. Journal of Alloys and Compounds, 2024, 1002: 175451.

[32] TAKAKI S. Effect of carbon and nitrogen on the Hall−Petch coefficient of ferritic iron (review on the Hall−Petch relation in ferritic iron) [J]. Materials Science Forum, 2010, 638/639/640/641/642: 168−173.

[33] QIN Peng-fei, YANG Qiang, GUAN Kai, MENG Fan-zhi, LV Shu-hui, LI Bai-shun, ZHANG Dong-dong, WANG Nan, ZHANG Jing-huai, MENG Jian. Microstructures and mechanical properties of a high pressure die-cast Mg−4Al−4Gd−0.3Mn alloy [J]. Materials Science and Engineering: A, 2019, 764: 138254.

[34] WANG Tao, ZHANG Mi-lin, NIU Zhong-yi, LIU Bin. Influence of rare earth elements on microstructure and mechanical properties of Mg−Li alloys [J]. Journal of Rare Earths, 2006, 24: 797−800.

[35] CHIA T L, EASTON M A, ZHU Su-ming, GIBSON M A, BIRBILIS N, NIE Jian-feng. The effect of alloy composition on the microstructure and tensile properties of binary Mg−rare earth alloys [J]. Intermetallics, 2009, 17: 481−490.

[36] QI Ming-fan, KANG Yong-lin, ZHU Guo-ming. Microstructure and properties of rheo-HPDC Al−8Si alloy prepared by air-cooled stirring rod process [J]. Transactions of Nonferrous Metals Society of China, 2017, 27: 1939−1946.

[37] LI X, XIONG S M, GUO Z P. Correlation between porosity and fracture mechanism in high pressure die casting of AM60B alloy [J]. Journal of Materials Science & Technology, 2016, 32: 54−61.

[38] HOU Ying-ying, WU Meng-wu, TIAN Bing-hui, LI Xiao-bo, XIONG Shou-mei. Characteristics and formation mechanisms of defect bands in vacuum-assisted high-pressure die casting AE44 alloy [J]. Transactions of Nonferrous Metals Society of China, 2022, 32: 1852−1865.

[39] WAN Li, HU Zu-qi, WU Shu-sen, LIU Xue-qiang. Mechanical properties and fatigue behavior of vacuum-assist die cast AlMgSiMn alloy [J]. Materials Science and

Engineering: A, 2013, 576: 252−258.
[40] ZHANG Yong-fa, ZHENG Jiang, XIA Ya-tong, SHOU Hao-ge, TAN Wei, HAN Wei-jian, LIU Qing. Porosity quantification for ductility prediction in high pressure die casting AM60 alloy using 3D X-ray tomography [J]. Materials Science and Engineering: A, 2020, 772: 138781.
[41] PAN Fu-sheng, CHEN Xian-hua, YAN Tao, LIU Ting-ting, MAO Jian-jun, LUO Wei, WANG Qin, PENG Jian, TANG Ai-tao, JIANG Bin. A novel approach to melt purification of magnesium alloys [J]. Journal of Magnesium and Alloys, 2016, 4: 8−14.
[42] WU Guo-hua, WANG Cun-long, SUN Ming, DING Wen-jiang. Recent developments and applications on high-performance cast magnesium rare-earth alloys [J]. Journal of Magnesium and Alloys, 2021, 9: 1−20.
[43] QIU Wei, LI Ya-wen, HUANG Gang, CHEN Jian, REN Yan-jie, HUANG Wei-ying, CHEN Wei, WU Tang-qing, YAO Mao-hai, XIONG Ai-hu. Corrosion behavior of as-cast AZ91 magnesium alloy with VN particle additions in NaCl solution [J]. Transactions of Nonferrous Metals Society of China, 2023, 33: 1398−1410.
[44] DARGUSCH M S, ZHU S M, NIE J F, DUNLOP G L. Microstructural analysis of the improved creep resistance of a die-cast magnesium–aluminium–rare earth alloy by strontium additions [J]. Scripta Materialia, 2009, 60: 116−119.
[45] UMAMAHESHWER RAO A C, VASU V, GOVINDARAJU M, SAI SRINADH K V. Stress corrosion cracking behaviour of 7xxx aluminum alloys: A literature review [J]. Transactions of Nonferrous Metals Society of China, 2016, 26: 1447−1471.
[46] LIU Wen-juan, CAO Fa-he, CHEN An-na, CHANG Lin-rong, ZHANG Jian-qing, CAO Chu-nan. Corrosion behaviour of AM60 magnesium alloys containing Ce or La under thin electrolyte layers. Part 1: Microstructural characterization and electrochemical behaviour [J]. Corrosion Science, 2010, 52: 627−638.
[47] GALICIA G, PÉBÈRE N, TRIBOLLET B, VIVIER V. Local and global electrochemical impedances applied to the corrosion behaviour of an AZ91 magnesium alloy [J]. Corrosion Science, 2009, 51: 1789−1794.
[48] LIU Wen-juan, CAO Fa-he, CHANG Lin-rong, ZHANG Zhao, ZHANG Jian-qing. Effect of rare earth element Ce and La on corrosion behavior of AM60 magnesium alloy [J]. Corrosion Science, 2009, 51: 1334−1343.
[49] DAI Jia-hong, JIANG Bin, PENG Cheng, PAN Fu-sheng. Effect of Mn additions on diffusion behavior of Fe in molten magnesium alloys by solid−liquid diffusion couples [J]. Journal of Alloys and Compounds, 2017, 710: 260−266.
[50] DINSDALE A T, QUESTED P N. The viscosity of aluminium and its alloys: A review of data and models [J]. Journal of Materials Science, 2004, 39: 7221−7228.
[51] ZHONG Wei, ZHAO Ji-cheng. Measurements of diffusion coefficients of Ce, Gd and Mn in Mg [J]. Materialia, 2019, 7: 100353.
[52] SHI Hui, HUANG Yuan-ding, LUO Qun, GAVRAS S, WILLUMEIT-RÖMER R, HORT N. A short review on diffusion coefficients in magnesium alloys and related applications [J]. Journal of Magnesium and Alloys, 2022, 10: 3289−3305.

用于超大型集成汽车部件的高压压铸 AM60 系合金的显微组织和性能

王 静[1,2]，郭 鑫[1,2]，宋江凤[1,2]，石荡赫[3]，谢何聪[1,2]，李春雨[1,2]，胡亨锐[1,2]，
陈 功[1,2]，蒋 斌[1,2]，向冬霞[4]，潘复生[1,2]

1. 重庆大学 国家镁合金材料工程技术研究中心，重庆 400044；
2. 重庆大学 先进铸造技术全国重点实验室，重庆 400044；
3. 赛力斯汽车有限公司 车辆技术部，重庆 401332；
4. 重庆先进轻金属研究院，重庆 400044

摘 要：采用含量低于 0.2%(质量分数)的 Mn、Ce 和 La 微合金化方法对商业 AM60 (Mg−6Al−0.3Mn)压铸镁合金进行改性。通过扫描电镜、透射电镜和显微 CT 等方法对 AM60 系合金的显微组织和力学性能进行表征。AM60-0.2La 合金表现出优异的力学性能，其极限抗拉强度、屈服强度和伸长率分别达到(288.0±1.7) MPa、(158.0±1.0) MPa 和(22.0±3.0)%。此外，在所研究的 4 种合金中，AM60-0.2La 合金的耐蚀性(0.29 mm/a)和流动性最好。其优异的力学性能和耐腐蚀性能主要归因于细晶强化、低孔隙率和低大缩孔含量，有望应用于超大型一体化汽车零部件。

关键词：镁合金；显微组织；力学性能；高压压铸；一体化汽车零部件

(Edited by Wei-ping CHEN)